Improving Point-Sensor Image Resolution with Distributed Acoustic Sensing at Brady's Enhanced Geothermal System

Samir F. JREIJ[1], Whitney J. TRAINOR-GUITTON[1], James L. SIMMONS[1], PoroTomo Team

[1]Dept. of Geophysics, Colorado School of Mines, 1500 Illinois St., Golden, CO, 80401

samirjreij@mymail.mines.edu

Keywords: distributed acoustic sensing, image resolution, active source, elastic reverse time migration

ABSTRACT

To date, investigations into the deployment and ability of surface horizontal distributed acoustic sensing (DAS) fiber to characterize reservoirs has been lacking compared to borehole DAS configurations, which has been more prevalent for well diagnostics and vertical seismic profiles. Existence of three-component (3C) geophones and surface DAS fiber at Brady's enhanced geothermal system motivates this study.

We review principles of compressional wave (P-wave) and shear wave (S-waves; SV and SH) particle motion and how these waves are recorded on horizontal DAS fiber as a function of their emergent angle. Note that vertical (P-wave) and orthogonal horizontal (S-wave) vibrators were used at Brady's making the consideration of S-waves potentially important.

We then use elastic synthetic prestack modeling and prestack elastic Reverse-Time-Migration (RTM) to explore the joint use of geophone and DAS data for subsurface seismic imaging. In particular, we use different combinations of the geophone and DAS data as input to RTM, and then document the extent to which the Brady fault model geometry is recovered by the imaging. The migrated images demonstrate that surface DAS can improve imaging resolution over that obtained from sparse geophones alone.

1. INTRODUCTION

Distributed acoustic sensing (DAS) is a technology that uses Rayleigh scattering in a fiber-optic cable to detect acoustic signals when the particle motion is parallel to the sensing fiber (Hornman et al., 2013). The two main components used in distributed sensing are the interrogator unit and the fiber-optic cable. Nearly any type of existing fiber-optic cable can be used in conjunction with an interrogator unit to record the acoustic signal.

Historically, DAS has been used in a borehole environment for flow monitoring, temperature measurements, and vertical seismic profiles (Mestayer et al., 2011; Barberan et al., 2012; Cox et al., 2012; Daley et al., 2013; Mateeva et al., 2014). Emphasis has been directed towards acquiring DAS in borehole environments, since many wells are already equipped with distributed sensors for production. As a result, acquiring DAS in boreholes is as simple as connecting the existing fiber-optic cable to a new interrogator unit that senses acoustic signal. Recently, Hornman (2017) compares the use of hydrophones to a helically wound fiber-optic cable.

A recent literature review reveals there have been no significant studies comparing surface geophones to horizontal DAS in active source surveys. We discuss the differences between surface DAS and 3C geophone data at Brady's Natural Lab, an enhanced geothermal system (Feigl et al., 2017).

Most recent papers in distributed acoustic sensing focus on how the system can be used without geophones. This is viable in a borehole environment due to the fact that the predominant particle motion of the recorded seismic data is in the vertical direction, parallel to the fiber. Surface horizontal DAS is sensitive to the horizontal component of particle motion. P-wave reflections will not be recorded on surface DAS at normal incidence, assuming a flat-layered earth, since the particle motion is vertical. As offset (incident angle) increases, the DAS fiber will sense the P-wave reflections. As offset increases, surface DAS arrays start to work very well. We can, recover a 1 meter spacing of virtual receivers along the DAS fiber which makes dense sampling arrays (Jreij et al., 2017). This is much denser that the original geophone array deployed at Brady's Natural Lab that has on average, a 100-meter receiver spacing. We show how surface distributed sensor arrays can improve imaging resolution when used in conjunction with sparse geophone arrays. Quantitative analysis of how frequently the faults are correctly imaged then describes if there is any added value using DAS sensors with 3C geophones.

1. Survey Design

The seismic survey was part of a larger experiment known as the Poroelastic Tomography by Adjoint Inverse Modeling of Data from Seismology, Geodesy, and Hydrology (or PoroTomo for short). This was a four-week experiment performed at Brady's Enhanced Geothermal System about twenty miles northwest of Fallon, Nevada. We address only the active source component of the experiment. Feigl et al. (2017) describes geodesy, hydrology, and passive seismic efforts in detail. The active source component consists of 238 3C geophones, 156 three-component vibroseis source locations (vertical and orthogonal horizontal vibrators), and nearly 9 km of surface fiber-optic cable (Figure 1). The vibroseis sweep is from 5 to 80 Hz.
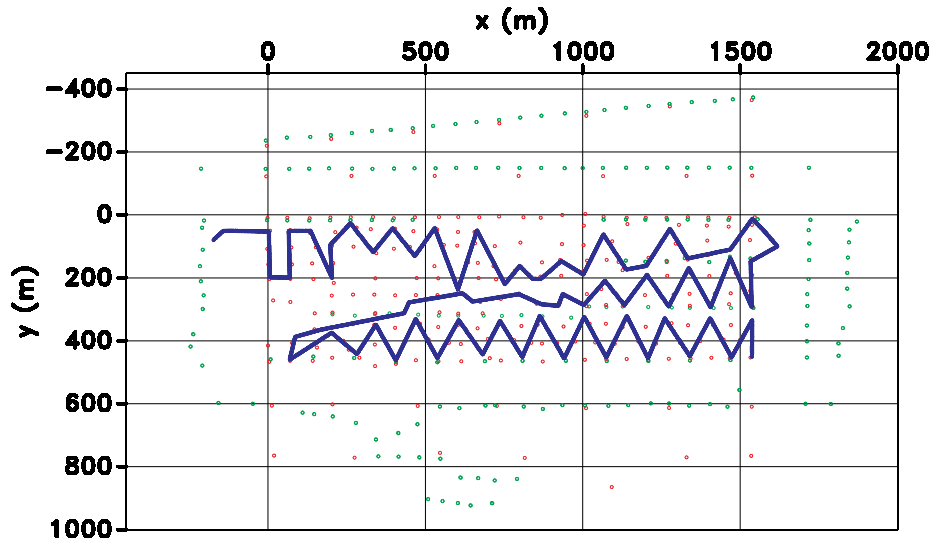
Figure 1: PoroTomo survey geometry where green dots are source locations, red dots are geophone locations, and the blue line is the DAS location.

2. FIBER ATTRIBUTES

Understanding how DAS fiber works is essential to working with the data that is currently available and for future surveys. Fiber is most sensitive to waves that have particle motion parallel to the orientation of the fiber. Every instrument has its own distinct sensitivity to the various types of waves depending on their emergent angle. The emergent angle (θ) represents the angle between the incoming wave and the surface of the Earth. An emergent angle of 0° represents a wave arriving parallel to the surface and an emergent angle of 90° represents a wave arriving perpendicular to the surface. A 3-C geophone, for example, has a sensitivity to waves, given the relevant component, that is proportional to $cos(\theta)$. DAS, on the other hand, considers only one horizontal component. DAS sensitivity decreases more rapidly than geophones as it has sensitivity that is proportional to $cos^2(\theta)$.

These points can be demonstrated with a simple 2-D example. Consider wave propagation in the x-z plane in a homogeneous, flat-layered, isotropic or vertical transverse isotropy medium (Figure 2). The horizontal DAS fiber is oriented in the x-direction. P-waves have particle motion parallel to the direction of wave propagation (Aki and Richards, 1980). Normal-incidence reflections from a horizontal reflector will arrive perpendicular to the surface fiber. In the case of a 2-D line of horizontal fiber with an inline P-source, the reflected P-wave will not be seen at short offsets. The particle motion of P-waves is parallel to the direction of propagation, so at short offsets, the reflected P-wave will arrive perpendicular to the fiber. As seen in Figure 3a, P-waves with a 0° emergent angle show 0 amplitude on fiber and maximum amplitude on the z-component of a geophone. Moving to further offsets yields emergent angles that are at a larger angle to the fiber. According to Figure 3a, these waves will show more data than waves arrive perpendicular to the fiber as they are propagating in the direction of the fiber and less data on the vertical component of the geophone. The further the offset, however, the lower the amplitude of the wave due to attenuation effects and Zoeppritz equations (Zoeppritz, 1919).

Shear-waves are potentially more interesting when recording with horizontal fiber. Consider again 2-D wave propagation in the x-z plane in a homogeneous, flat-layered, isotropic or vertical transverse isotropy medium (Figure 2). SV-waves have particle motion in the x-z plane, as do P-waves (Aki and Richards, 1980). Normal-incidence reflections from a horizontal reflector will arrive perpendicular to the surface fiber. P-wave particle motion, as stated previously, will be in the z direction, and consequently, will not be recorded by the fiber. SV wave particle motion will be in the x-direction, and the DAS response will be maximum (Figure 3b). Although one may consider using a P-source and DAS to record short offset SV-reflections, the reflections for these converted events have low amplitudes (Zoeppritz,1919). At larger offsets, the SV-wave emerging angle begins to approach 90°. A larger emerging angle means less signal (Figure 3b) is recorded by both the surface DAS and the x-component of the geophone because the SV-wave particle motion approaches perpendicular to these components (Figure 2).

We also consider using SH-waves with the same 2-D survey geometry (homogeneous, flat-layered, isotropic). SH-waves propagate in the x-z plane. SH waves have particle motion perpendicular to the direction of wave propagation or, in this case, in the y-direction. The SH-DAS response will be zero since the SH particle motion is perpendicular to the DAS fiber in the y-direction. In this 2-D case, the SH-wave will be out of plane regardless of source-receiver offset. In 3-D, SH-waves can be seen on the DAS if it is properly oriented. For example, a source-receiver azimuth perpendicular to the 2-D fiber (in this case, in the y-direction) will produce a maximum amplitude reflection on the DAS since the particle motion is in the x-direction for all offsets. As the source-receiver azimuth moves inline with the fiber, the SH-wave particle motion decreases, and is equal to zero when the source-receiver azimuth is inline with the fiber.
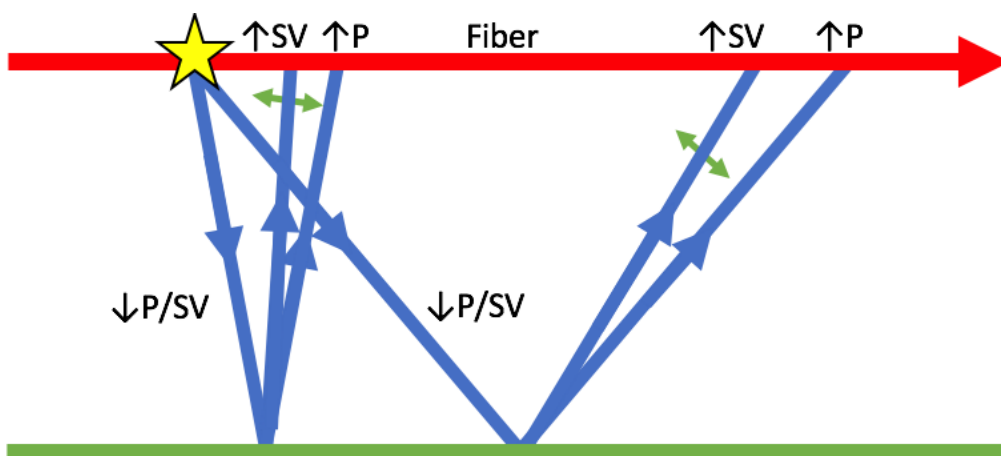
Figure 2: Demonstration of P-P wave effect on fiber using ray paths. The blue lines represent ray paths of the labeled wave. The blue arrows represent the direction of the wave. The green line represents a horizontal reflector in the subsurface. The yellow star represents the source.


(a)

(b)
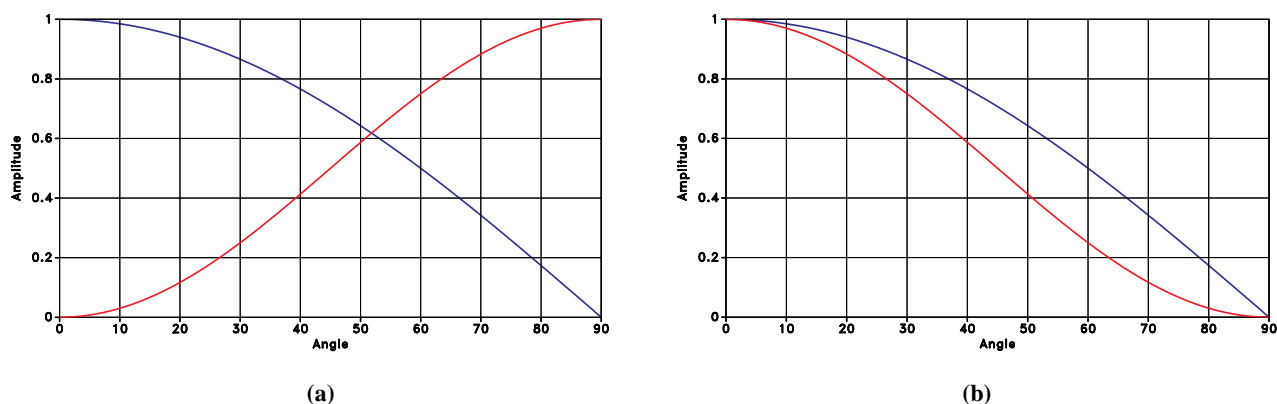
Figure 3: Amplitude versus emerging angle for both geophone (blue) and horizontal DAS (red). An emerging angle of 0 degrees indicates a wave that is propagating perpendicular to the surface and an emerging angle of 90 degrees indicated a wave is propagating parallel to the surface. (a) Sensitivity with respect to a P-wave at different emerging angles of horizontal DAS (red) and geophone z-component (blue). (b) Sensitivity with respect to an SV-wave at different emerging angles of horizontal DAS (red) and geophone x-component (blue).

2.1 Resulting Geometry Issues

As discussed earlier, the PoroTomo active source survey consisted of 240 multi-component geophones and nearly 9 km of surface DAS cable trenched horizontally. The source used for the survey was a 64,000-pound shaker from the University of Texas. The geometry of the survey is shown in Figure 1. The maximum offset in the survey was 1,500 meters. This short offset and insufficient sampling (i.e. 100-meter average geophone spacing) proved to be a major obstacle in seismic processing. In land data, ground roll is difficult to attenuate and recover the signal encrypted by it. At such short offsets, nearly all the P-wave data is covered by ground roll. With a dense set of geophones, attenuating the ground roll is a routine processing step. With a sparse receiver configuration (such as the PoroTomo acquisition), attenuating ground roll is a more difficult task.

Figure 4a shows a 2-D receiver line at 75-meter receiver spacing with an inline source. The target depth of interest (depths of Brady's enhanced geothermal system) ranges from 150 – 600 meters (Feigl et al., 2017). Identifying ground roll to attenuate in this data is a difficult task because the receiver spacing is large. Reflection events in the target depths are encrypted by the ground roll. Looking at the data in terms of all the receivers in offset fills in some of the holes of the 2-D line (Figure 4b). Shallow reflection events are challenging to follow as they are near horizontal with the offsets that are present and the large amount of noise present in the data (Figure 4b). For all these reasons, a synthetic study testing the feasibility of combining DAS and multi-component geophones is conducted in this paper for future surveys.
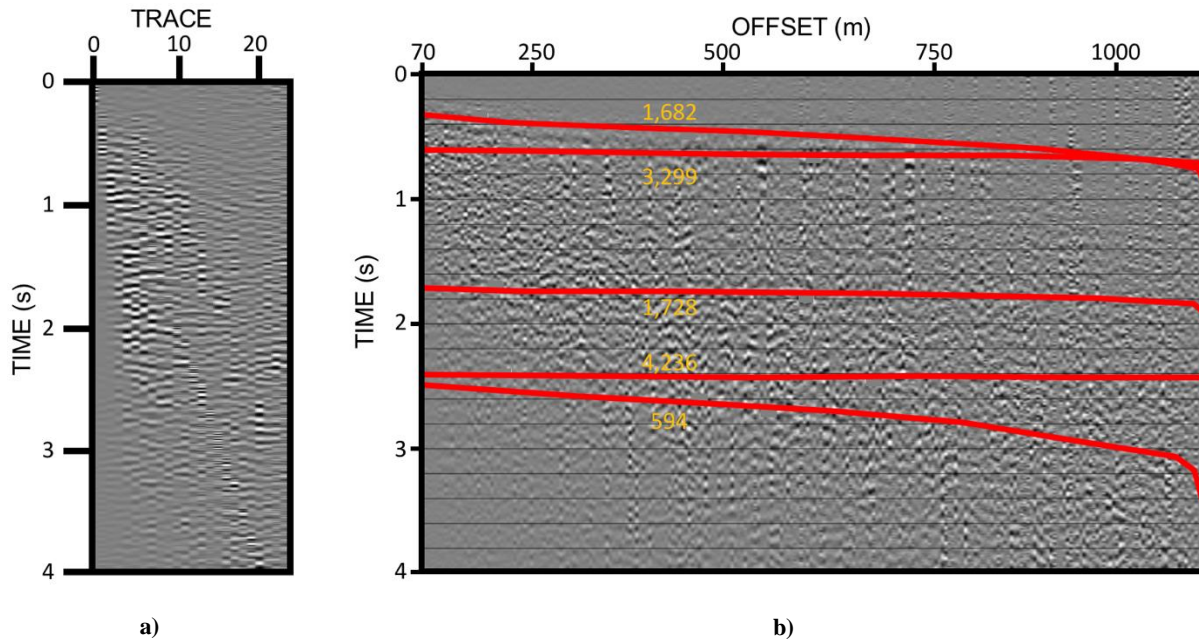
Figure 4: (a) Shot 51 on the PoroTomo Survey along a 2-D geophone line. The geophone data is encrypted by ground roll and reflection events are not present. (b) Looking at all of the geophone data against offset provides insight on where we might see reflection events given a certain NMO (normal moveout) velocity. The orange numbers represent NMO velocities in meters/second. It is difficult to see any moveout given the acquisition parameters.

3. METHODOLOGY

Imaging the geophone data is a difficult task in the PoroTomo survey due to the insufficient spatial sampling and offset. This paper focuses on identifying a way to resolve the spatial sampling issue. Fortunately, the PoroTomo survey includes horizontal DAS cable that has 10-meter gauge length and an equivalent of 1-meter receiver spacing along the fiber. Many papers in the literature are interested in methods to convert DAS measurements (strain or strain rate) to a geophone equivalent (particle velocity or displacement) with the intent to replace point sensors with distributed sensors or use existing geophone processing to clean up DAS data (Daley et al, 2015; Jreij et al., 2017). We explore the idea of using both data types simultaneously to produce more detailed images using synthetic examples.

3.1 2-D Synthetic Design

Siler and Faulds (2013) mapped the faults of Brady's Natural Lab. It is important to image these faults in detail as they are the driving factors behind the recharge of the geothermal reservoir (Feigl et al., 2017). For this reason, we used a slice from the fault model of Brady's Natural Lab (Siler and Faulds, 2013) extracted from the location of Well 56-1A in the PoroTomo Survey as a reflection velocity model (Figure 5a). This well is significant as it includes a borehole DAS cable that is also used for imaging by other collaborators (Trainor-Guitton et al., 2018).

In the first example, we use 2-D elastic forward modeling to produce strain and displacement data along the surface of our 2-D example excited by a P-source. We record with receivers at every 1-meter. This is then decimated to 100 meters spacing to replicate the PoroTomo geometry of geophones along the long axis of the PoroTomo survey. The geophones recorded the displacement for the Z and X-axes. Strain is recorded in between the geophones to imitate what a fiber would record. The strain, however, is only recorded along the X-axis as there is only a single component fiber in the PoroTomo survey. Then, acceleration sources were placed along the surface of the experiment at 100 meters spacing.

The second example is similar to the first example: the same geometry is used, except an S-Source is used to generate data. The same geometry is used in conjunction with an S-Source. As stated in section 2, fiber is sensitive to waves with particle motion parallel to the fiber direction. P-waves can also be converted to S-waves at reflection boundaries, but this experiment was conducted to see if new information can be acquired by a S-source.

The third experiment model involved the short axis (e.g. shorter total aperture) of the fault model (Siler and Faulds, 2013) extracted at Well 56-1A (Figure 7a). The new model consists of higher dip events to test the aperture of the PoroTomo survey. The short axis of the PoroTomo survey was only approximately 900-meters in length. The same source and receiver spacing from the first two experiments were used.

We use elastic imaging, specifically reverse time migration, as a technique to compare the different data types and their combination. In specific, elastic reverse time migration is used. Using an acceleration source, we forward model data from the reflection fault model slice on both the geophones and the fiber cable. The direct wave is subtracted from this data by creating data in the same model without

reflections. A forward wavefield is computed with a smooth velocity model so there are no reflections. This is used as the source wavefield for the geophones in the reverse time migration. The geophone data without the direct wave is reinjected in reverse at the nodal receiver locations as an acceleration source to produce a geophone receiver wavefield. For the strain data, the direct wave is removed just as it is in the geophone data. The source wavefield is the same wavefield that is used for the geophone data. The receiver wavefield, however, is produced differently. The strain data without the direct wave is reinjected in reverse at the fiber locations, but now it is reinjected as a stress source.

3.2 Energy Norm Imaging Condition

An imaging condition is needed to produce images from these wavefields. The energy norm imaging condition is utilized for this experiment (Rocha et al., 2015). The resulting images from both the fiber and geophones are then stacked over experiment and data type. Conventional imaging conditions for reverse time migration rely on taking the inner product of source and receiver wavefields at each spatial location (Claerbout, 1971). The energy norm imaging condition relies on the energy conservation principle. The imaging condition is shown in Equation 1, where U is the source wavefield oriented forward in time, V is the receiver wavefield oriented backwards in time, and λ and μ are the Lamé parameters.

$$I_E = \sum_{e,t} \left[\rho \dot{U} \cdot \dot{V} + (\lambda + \mu)(\nabla \cdot U)(\nabla \cdot V) + \mu(\nabla U):(\nabla V) \right]$$

(1)

This imaging condition outputs an image that represents the total reflection energy from extrapolated wavefields (Rocha et al., 2015). There are various benefits to using this imaging condition, but the most important for the experiments in this paper is the reduction of images from the conventional 4 images (PP, PS, SP, SS) to 1 finalized elastic image.

4. RESULTS

The results of the different experiments are presented below (Figures 5-7) in the form of the multi-component geophone image, the DAS image, and the result of combining the two different images.

Figure 5 shows the results of migrating geophone (b), DAS data (c), and the combination (d) using a vertical source to generate the data. Figure 5a is the original model that produced the data for the migration. This data represents a slice of Siler and Faulds (2013) fault model at well 56-1A along the long axis of the PoroTomo survey. The image from using only the multi-component geophone data (5b) shows reflectors that are discontinuous and difficult to follow. The image is also covered with migration artifacts due to insufficient sampling of the wavefield. An example of this is presented at around .8 km on the x-axis of Figure 5b: the migration artifacts make it difficult for an interpreter to follow the shallow reflector. The deeper reflector is difficult to identify in Figure 5b. The DAS image (Figure 5c) shows a crisp and continuous image of the shallow reflector. Although migration artifacts are experienced around .8 km on the x-axis, these are different from those experienced in Figure 5b. These migration artifacts are due to fake modes present because the wavefield is extrapolated using only the x-component at the surface. Now there are two images with two different migration artifacts (types of noise). The power of stacking the images should theoretically eliminate the noise and highlight the reflection events. Linearly stacking the events, however, will not work as the amplitudes are on different scales. Both images are normalized by amplitude and then stacked to produce Figure 5d. Although Figure 5d still has artifacts in it, the reflectors are enhanced and the image is easier to interpret than Figures 5b-c.
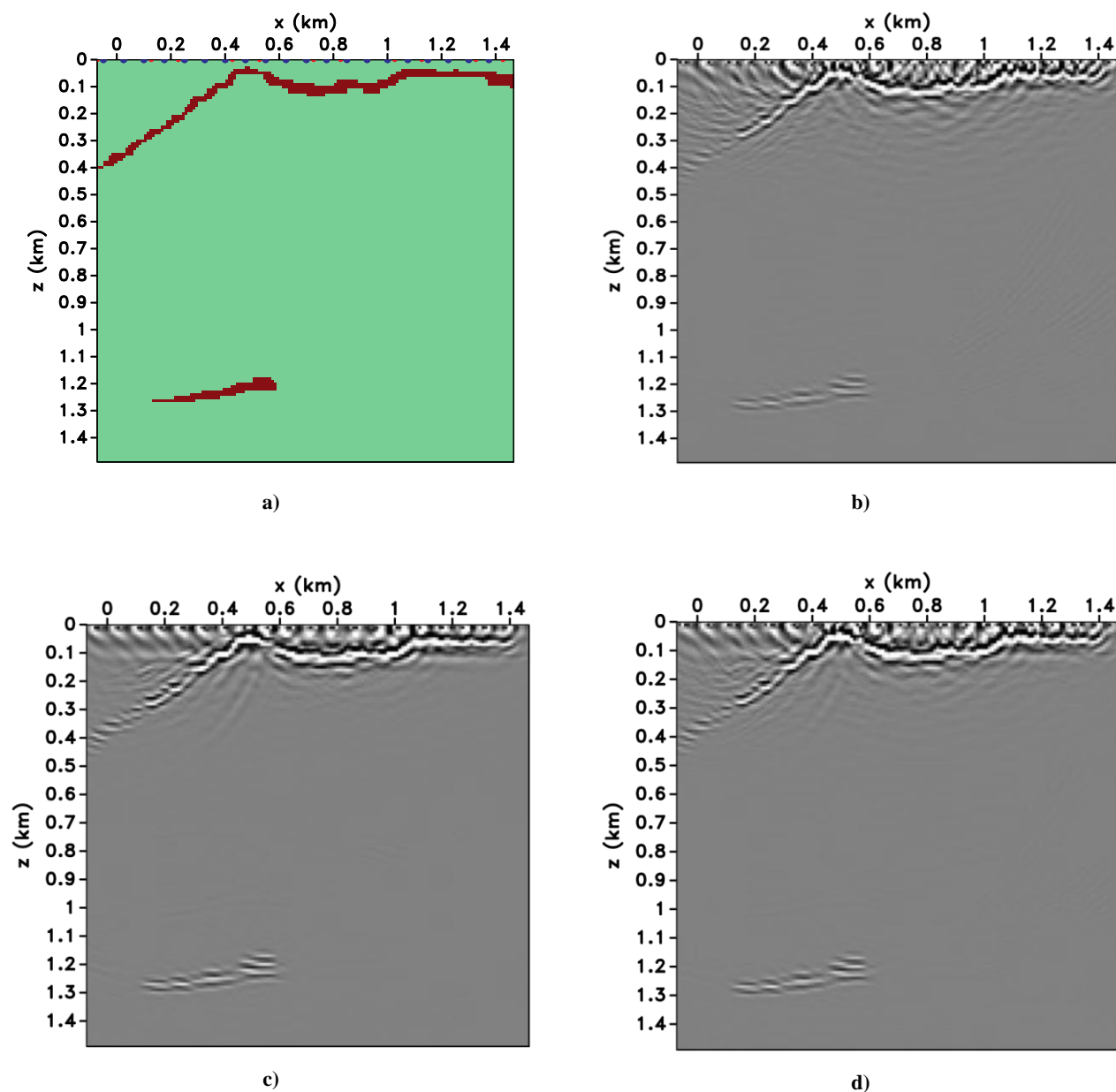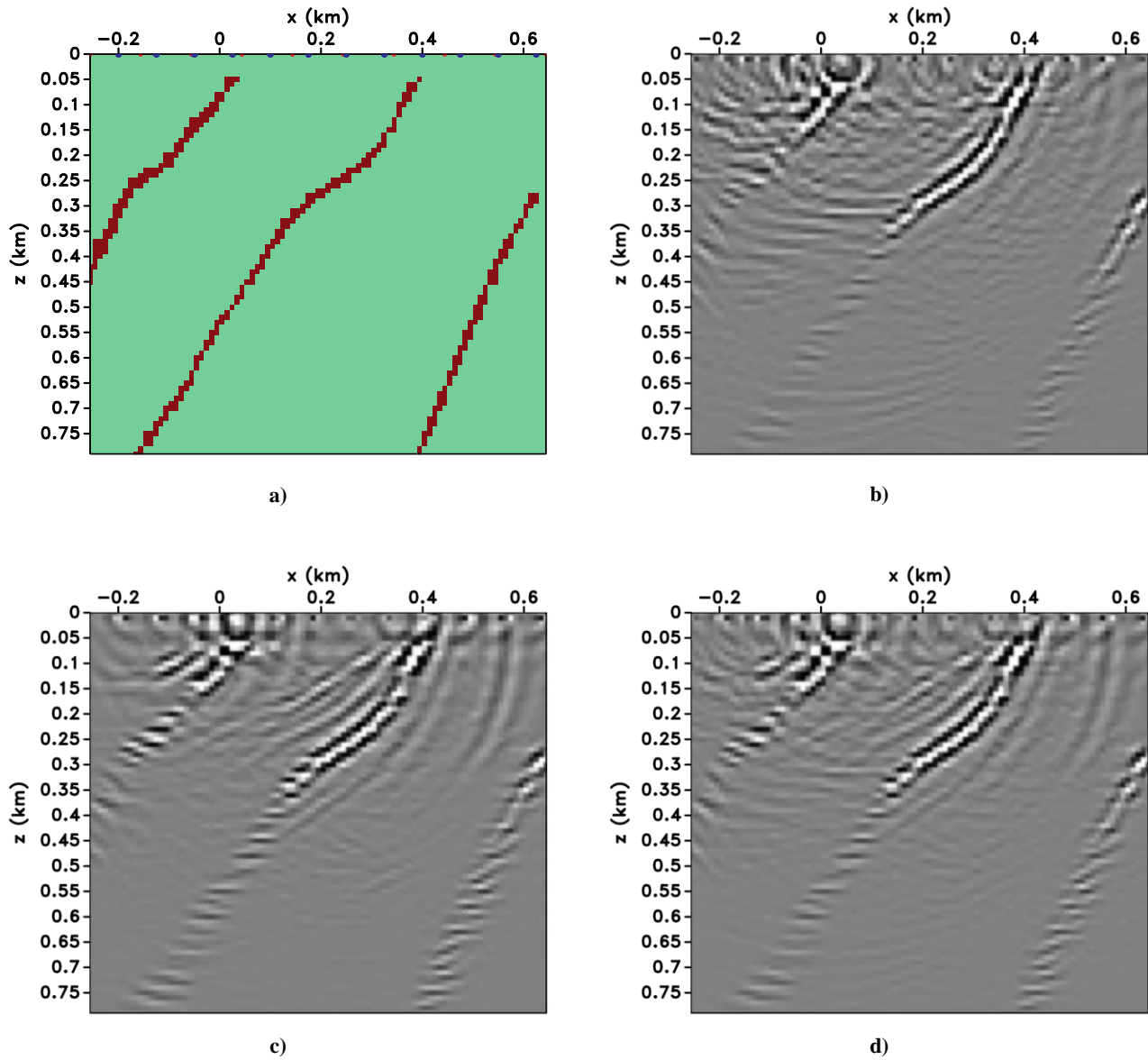

a)

b)
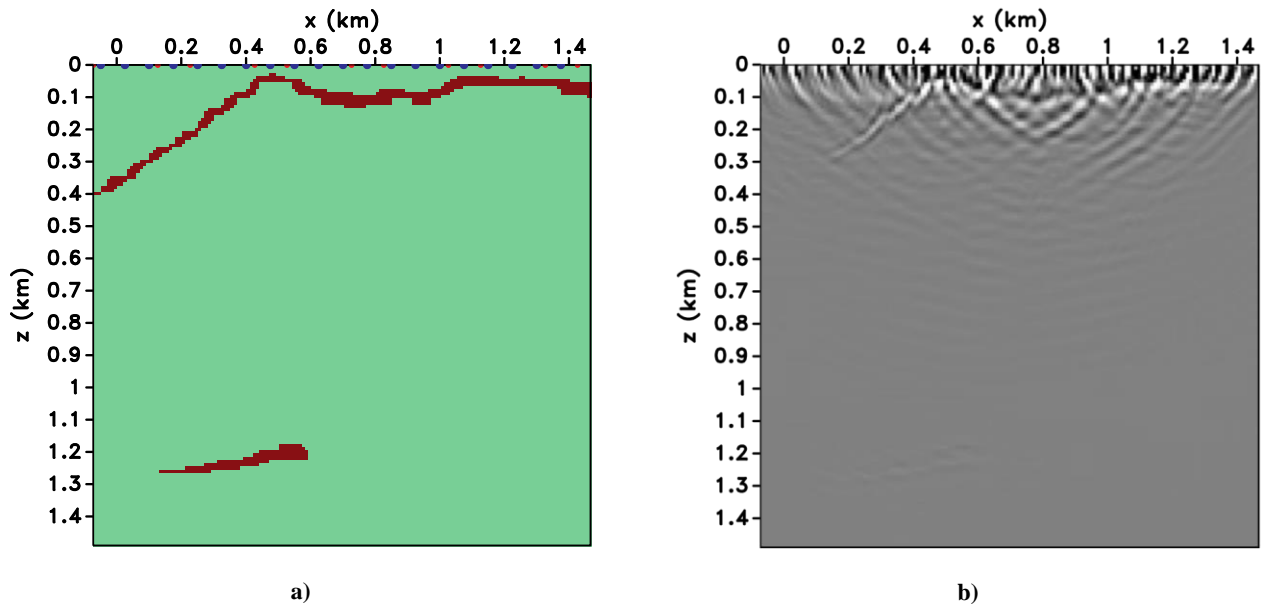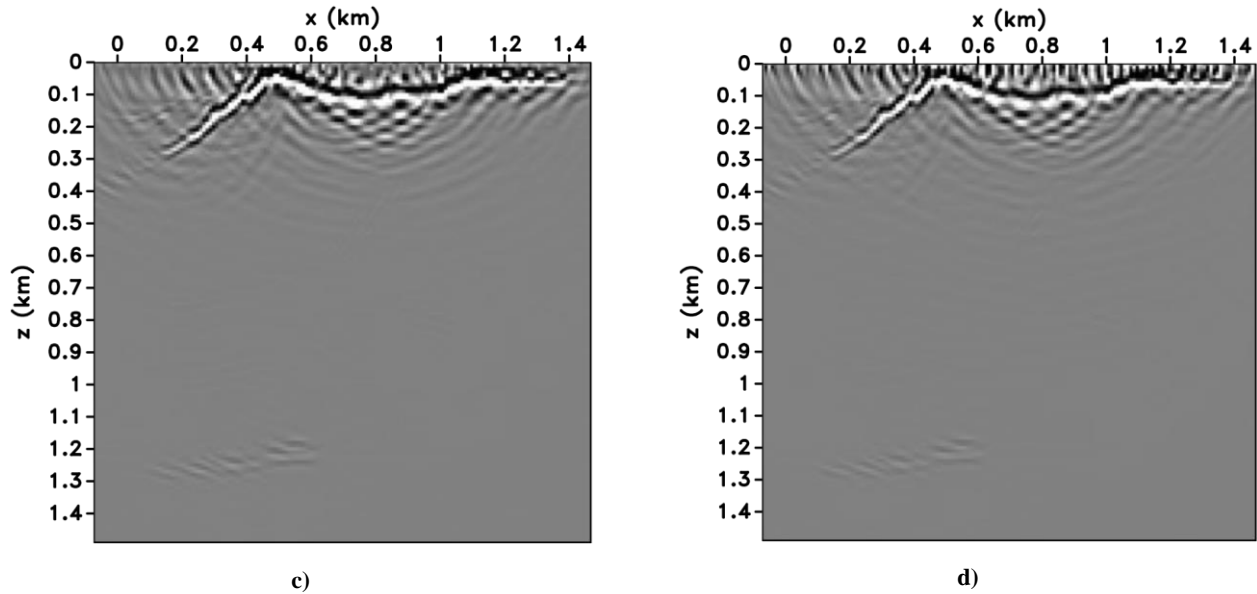
Figure 5: (a) Fault reflectivity model slice from Siler and Faulds (2013) at the location of well 56-A1. Blue dots represent source locations and red dots represent geophone locations. DAS fiber was placed between the geophone locations. (b) Resulting image from migrating geophone synthetic data. (c) Resulting image from migrating DAS synthetic data. (d) Combined image from migrating DAS and geophone synthetic data.

Figure 6 shows the results of migrating geophone and DAS data using a horizontal source to generate the data. The image from using only the multi-component geophone data (Figure 6b) shows reflectors that are still discontinuous, but now the image is easier to follow. The receiver sampling was not changed, so the image is still covered with migration artifacts due to insufficient sampling of the wavefield. On the left-hand side of the geophone image, we can see that the end of the dipping fault is not properly imaged. This is due to insufficient aperture in the migration. The deeper reflector is now easier to identify in Figure 6b. The DAS image (Figure 6c) is still very crisp, but now the migration artifacts have diminished. The images are normalized and stacked again to produce Figure 6d. Figure 6d shows reflectors clearer than Figure 5d, suggesting that a horizontal force would work in imaging the faults in the PoroTomo area.

Figure 7 shows the results of migrating geophone and DAS images with a new reflectivity model as it is a slice from the short PoroTomo axis at the location of Well 56-1A (Figure 7a). A horizontal source was used for this experiment as it had the best results in the previous experiments. Migration artifacts are largely present in the geophone image (Figure 7b), but the reflectivity model is reconstructed in the shallow zone (depths up to 350 meters). The aperture is not wide enough to image the fault reflections below this point. The DAS image (Figure 7c) does not have the continuous reflections that Figure 7b has. The reasons for this are the wave mechanics and aperture discussed previously. The S-waves will show on the DAS fiber at larger offsets. In this case, the large offsets are not present because the experiment was limited by the offsets in the PoroTomo survey. Nevertheless, we can still normalize and stack the images to reduce the migration artifact effects (Figure 7d).
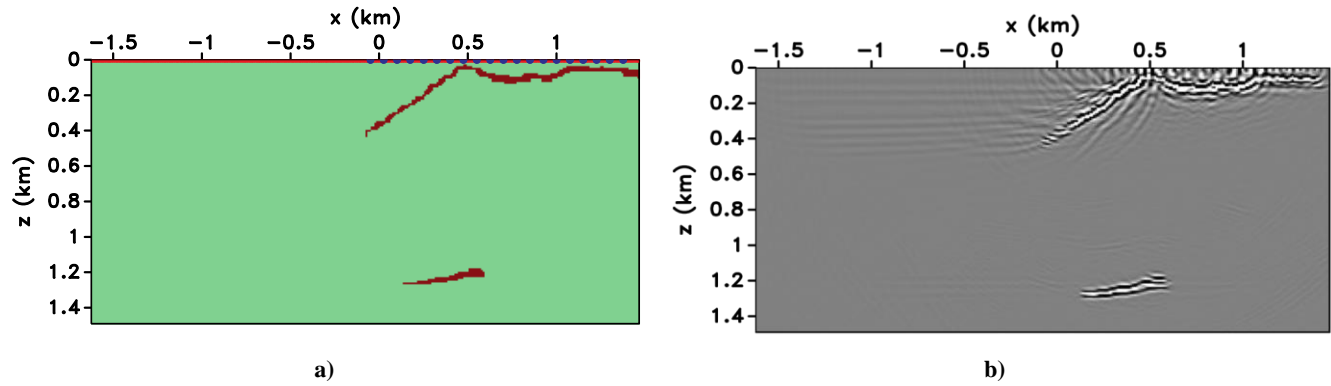
Figure 6: (a) Fault reflectivity model slice from Siler and Faulds (2013) at the location of well 56-A1. Blue dots represent source locations and red dots represent geophone locations. DAS fiber was placed between the geophone locations. (b) Resulting image from migrating geophone synthetic data. (c) Resulting image from migrating DAS synthetic data. (d) Combined image from migrating DAS and geophone synthetic data.

Figure 7: (a) Fault reflectivity model slice from Siler and Faulds (2013) at the location of well 56-A1. Blue dots represent source locations and red dots represent geophone locations. DAS fiber was placed between the geophone locations. (b) Resulting image from migrating geophone synthetic data. (c) Resulting image from migrating DAS synthetic data. (d) Combined image from migrating DAS and geophone synthetic data.

Aperture has been mentioned many times as an issue with the survey parameters. An extended model (Figure 8a) was created to demonstrate the effects of increasing aperture. The source placement was kept the same as previous experiments (red dots on Figure 8a), but now the DAS receivers were extended to cover the large offsets. A horizontal force is used as the source mechanism. The image resulting from migrating the DAS data is presented in Figure 8b. Figure 8b highlights the sharp reflectors better than Figure 6c and almost perfectly reconstructs the model. Aperture should be kept in mind for future 2-D and 3-D surveys with surface distributed sensors.

Figure 8: (a) Fault reflectivity model slice from Siler and Faulds (2013) with increased aperture. Blue dots represent source locations and red dots represent geophone locations. DAS fiber was placed between the geophone locations. (b) Resulting image from migrating DAS synthetic data.

4.1 Value of Information

All of the experiments presented in the paper can be qualitatively analyzed and discussed, but qualitative analysis is always different between people due to different biases. A method to quantitatively analyze the experiments is needed to do comparisons. Value of Information is a quantitative tool that originates from the field of decision analysis to quantify how relevant and reliable an information source is (Trainor-Guitton et al., 2013). VOI estimates the possible increase in expected utility by gathering information. It is calculated by subtracting the prior value of information and the value with data (Equation 2). The goal of this project is to observe if there is any added value to using distributed acoustic sensing in surface acquisitions.

$$VOI = V_{w/\,data} - V_{prior} \tag{2}$$

A methodology to bring out the reflection events must be implemented to assess the posterior value of the datasets (Equation 3). As we discussed in section 3.2, the resulting image from energy norm reverse time migration represents the total amount of energy reflected in the subsurface. In theory, the largest amplitudes from this image will be reflection events. In the case of this experiment, the reflection events represent the faults that we are trying to image. An amplitude filter is used as a first pass to bring out reflections in the dataset. Every model cell that is above the applied limit is assigned a value of 1 and every model box that is below the limit is assigned a value of 0. For example, the image in Figure 6b shows that the maximum absolute amplitude is about 500,000. The top 80%, 90% and 95% of the reflected energy are filtered on the image to highlight areas where reflections are coming from as opposed to migration artifacts (Figure 9a-c). Although the results in Figure 9 are not perfect representations of where interpreters would place the faults, this approach represents the beginning steps to quantify the value added by DAS fiber over sparse geophones.
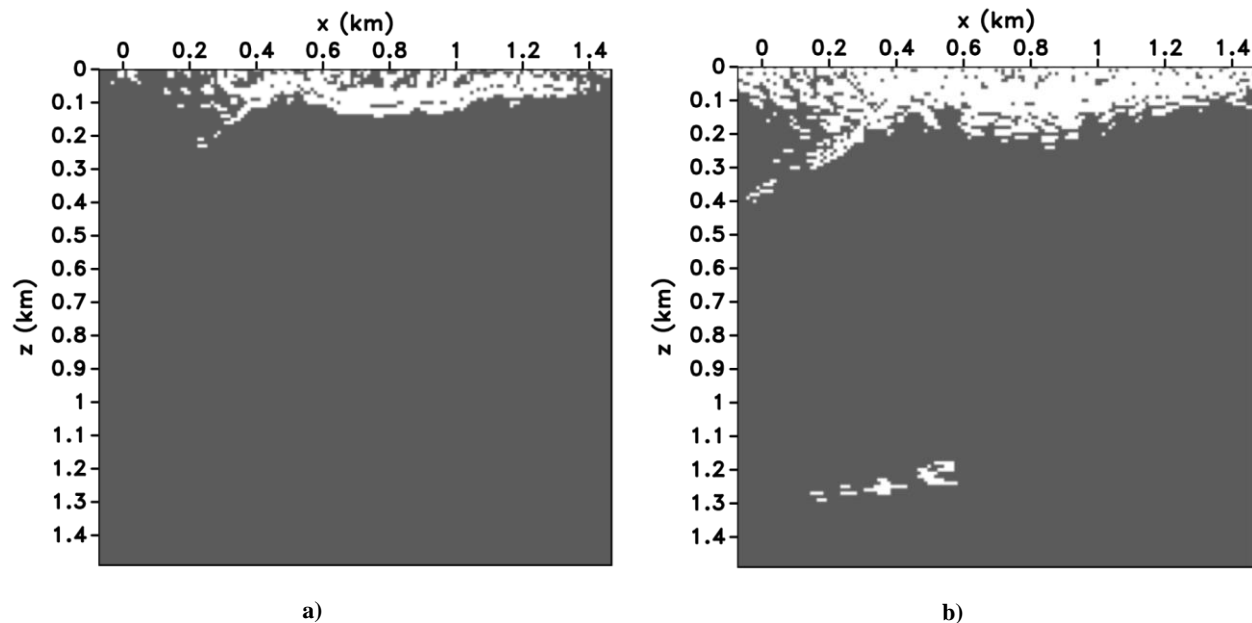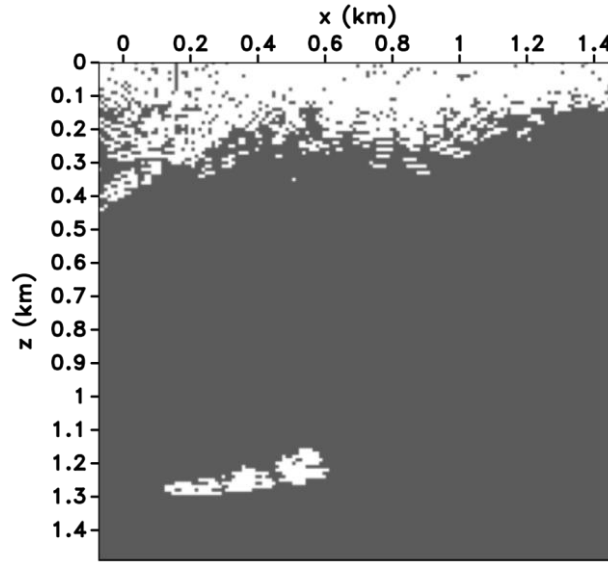
c)

Figure 9: (a) Reflections amplitudes that represent the top 80% of energy recorded. (b) Reflection amplitudes that represent the top 90% of energy recorded. (c) Reflection amplitudes that represent the top 95% of energy recorded.

A cell-by-cell comparison between the filtered energy images (Figures 9a-c) and the original fault image (Figure 5a) is performed to identify how accurate both technologies are able to identify features in the fault model. The results of this cell-by-cell comparison are presented in confusion matrix form (Tables 1-3). A confusion matrix is table that is used to describe performance on a set of test data for which the true value is known. The term Θ_F denotes that a known fault exists and the term Θ_{NF} denotes that no known fault exists. The terms Θ_F^{int} and Θ_{NF}^{int} represent the interpretation that fault exists or doesn't exists based on filtering of energy images. The columns of the confusion matrix represent predicted classifications (Θ_F^{int} and Θ_{NF}^{int}). The rows of the confusion matrix represent actual true statement of the subsurface (Θ_F and Θ_{NF}).

Table 1: Confusion matrix for Figure 7b with top 80% energy reflected.		
	Θ_F^{int}	Θ_{NF}^{int}
Θ_F	231	415
Θ_{NF}	499	22105

Table 2: Confusion matrix for Figure 7b with top 90% energy reflected.		
	Θ_F^{int}	Θ_{NF}^{int}
Θ_F	307	336
Θ_{NF}	922	21685

Table 3: Confusion matrix for Figure 7b with top 95% energy reflected.		
	Θ_F^{int}	Θ_{NF}^{int}
Θ_F	371	269
Θ_{NF}	1451	21159

The confusion matrices allow us to calculate posterior values using Equation 3.

$$\Pr\left(\theta = \theta_i \middle| \theta^{int} = \theta_j\right) = \frac{\Pr(\theta=\theta_i)\,\Pr(\theta^{int}=\theta_j|\theta=\theta_i)}{\Pr(\theta^{int}=\theta_i)};\ \forall\ i,j = \{F, NF\} \tag{3}$$

The posterior value explains the probability that the event which the data type predicted is actually the event that is present. These are used to calculate the value with information (data) shown in Equation 2. The results for the posterior values are displayed in Table 4. In every experiment, adding distributed sensors increases the probability of finding if a cell is a fault/not a fault and decreases the probability of false positives/false negatives.

Table 4: Posterior reliability of information calculated using Equation 3 for all of the experiments.

	Vertical Source Geophone only	Vertical Source Geophone & DAS	Horizontal Source Geophone only	Horizontal Source Geophone & DAS	Crossline Fault Model Geophone Only	Crossline Fault Model Geophone & DAS
$\Pr(\theta = \theta_F \mid \theta^{int} = \theta_F)$	0.315 %	0.46 %	0.880 %	0.917 %	0.957 %	1.00 %
$\Pr(\theta = \theta_F \mid \theta^{int} = \theta_{NF})$	86.24 %	81.0 %	66.46 %	65.08 %	75.51 %	74.35 %
$\Pr(\theta = \theta_{NF} \mid \theta^{int} = \theta_F)$	0.069 %	.064 %	0. 051 %	0.050 %	0.20 %	0.189 %
$\Pr(\theta = \theta_{NF} \mid \theta^{int} = \theta_{NF})$	94.82 %	94.97 %	95.43 %	95.49 %	91.34 %	91.49 %

5. CONCLUSIONS

This paper has detailed the types of data that surface distributed sensors are able to record. DAS has shown to be useful in a 2-D surface array as long as there is clean, processed data available. Assuming the prior survey contains a sparse array of geophones, we have shown that imaging with a combination of distributed sensors and geophones proves to be useful. We have shown that using distributed sensors in a 2-D line proves to add value by evaluating the posterior information reliability.

6. FUTURE WORK

In the future, this experiment will be extended to a 3-D survey. As we move to 3-D, more waves will be observed as the fiber in the PoroTomo survey included different azimuths. It will be useful to test imaging with the DAS array using other types of sources (i.e. SH and SV sources).

A more accurate value of information study must be conducted for seismic imaging as this one does not take into account artifacts. The energy norm imaging condition produces amplitudes that are based on the energy of reflected events. In this paper, we simply took an amplitude limits as an interpretation of the events. We do not take into account that a geophysicist would not pick energy from artifacts to be reflection events. A more sophisticated algorithm will need to be implemented to account for this.

Jreij et. al.

REFERENCES

Aki, K. and Richards, P. G., 1980, Quantitative seismology: Theory and methods, v. l: W.H. Freeman and Co.

Barberan, C., C. Allanic, D. Avila, J. Hy-Billiot, A. Hartog, B. Frignet, and G. Lees, 2012, Multi-offset seismic acquisition using optical fiber behind tubing: 74th Annual International Conference and Exhibition, EAGE, Extended Abstracts.

Claerbout, J., 1971, Toward a unified theory of reflector mapping: Geophysics, v. 36, p. 467–481.

Cox, B., P. Wills, D. Kiyashchenko, J. Mestayer, J. Lopez, S. Bourne, R. Lupton, G. Solano, N. Henderson, D. Hill, and, J. Roy, 2012, Distributed acoustic sensing for geophysical measurement, monitoring and verification: Canadian Society of Exploration Geophysicists, v. 37, p. 7–13.

Daley, T. M., B. M. Freifeld, J. Ajo-Franklin, S. Dou, R. Pevzner, V. Shulakova, S. Kashikar, D. E. Miller, J. Goetz, J. Henninges, and, S. Lueth, 2013, Field testing of fiber-optic distributed acoustic sensing (das) for subsurface seismic monitoring: The Leading Edge, v. 32, p. 699–706. doi: 10.1190/tle32060699.1

Daley, T.M., Miller, D.E., Dodds, K., Cook, P., and Freifeld, B.M., 2015, Field testing of modular borehole monitoring with simultaneous distributed acoustic sensing and geophone vertical seismic profiles at Citronelle, Alabama: Geophysical Prospecting, p. 1–17, doi: 10.1111/1365-2478.12324.

Feigl, K. L., 2017, Overview and preliminary results from the PoroTomo project at brady hot springs, Nevada: Poroelastic tomography by adjoint inverse modeling of data from seismology, geodesy, and hydrology: Presented at the Stanford Geothermal Workshop.

Jreij, S. F., Trainor-Guitton, W. J., Miller, D., 2017, Field data comparison of 3D horizontal distributed acoustic sensing and geophones: Society of Exploration Geophysicists Technical Program Extended Abstracts 2017, p. 1-6.

Hornman, J., 2017, Field trial of seismic recording using distributed acoustic sensing with broadside sensitive fibre-optic cables: Geophysical Prospecting, v. 65, p. 35–46, doi: 10.1111/1365- 2478.12358.

Hornman, K., B. Kuvshinov, P. Zwartjes, and A. Franzen, 2013, Field trial of a broadside-sensitive distributed acoustic sensing cable for surface seismic: 75th Annual International Conference and Exhibition, EAGE, Extended Abstracts.

Mateeva, A., Lopez, J., Potters, H., Mestayer, J., Cox, B., Kiyashchenko, D., Wills, P., Grandi, S., Hornman, K., Kuvshinov, B., Berlang, W., Yang, Z., and Detomo, R., 2014, Distributed acoustic sensing for reservoir monitoring with vertical seismic profiling: v. 62, p. 679–692, doi: 10.1111/1365-2478.12116.

Mestayer, J., B. Cox, P. Wills, D. Kiyashchenko, J. Lopez, M. Costello, S. Bourne, G. Ugueto, R. Lupton, G. Solano, and, D. Hill, 2011, Field trials of distributed acoustic sensing for geophysical monitoring: 81st Annual International Meeting, SEG, Expanded Abstracts, p. 4253–4257, doi :10.1190/1.3628095.

Plesinger, A., Hellweg, M. and Seidl, D., 1986, Interactive high-resolution polarization analysis of broad-band seismograms. Journal of Geophysics, v. 59, p.129-139.

Siler, D.L., and Faulds, J.E., 2013, Three-Dimensional Geothermal Fairway Mapping: Examples From the Western Great Basin , USA: GRC Transactions, v. 37, p. 327–332.

Trainor-Guitton, W.J., Ramirez, A., Yang, X., Mansoor, K., Sun, Y., and Carroll, S., 2013, Value of information methodology for assessing the ability of electrical resistivity to detect CO2/brine leakage into a shallow aquifer: International Journal of Greenhouse Gas Control, v. 18, p. 101–113, doi: 10.1016/j.ijggc.2013.06.018.

Trainor-Guitton, W. J., Jreij, S.F., Simmons, J., 2018, 3D Imaging from vertical DAS fiber at Brady's Natural Laboratory: *Proceedings*, 43rd Workshop on Geothermal Reservoir Engineering, Stanford University, Stanford, CA.

Zoeppritz, K. and Erdbebnenwellen, V., 1919, On the reflection and penetration of seismic waves through unstable layers. Göttinger Nachrichten, I, pp.66-84.